UC San Diego
UC San Diego Previously Published Works

Title
Interannual variations in meltwater input to the Southern Ocean from Antarctic ice shelves.

Permalink
https://escholarship.org/uc/item/6zp1r90c

Journal
Nature geoscience, 13(9)

ISSN
1752-0894

Authors
Adusumilli, Susheel
Fricker, Helen Amanda
Medley, Brooke
et al.

Publication Date
2020-09-01

DOI
10.1038/s41561-020-0616-z

Peer reviewed

Interannual variations in meltwater input to the Southern Ocean from Antarctic ice shelves

Susheel Adusumilli [1✉], Helen Amanda Fricker[1], Brooke Medley [2], Laurie Padman [3] and Matthew R. Siegfried [4]

Ocean-driven basal melting of Antarctica's floating ice shelves accounts for about half of their mass loss in steady state, where gains in ice-shelf mass are balanced by losses. Ice-shelf thickness changes driven by varying basal melt rates modulate mass loss from the grounded ice sheet and its contribution to sea level, and the changing meltwater fluxes influence climate processes in the Southern Ocean. Existing continent-wide melt-rate datasets have no temporal variability, introducing uncertainties in sea level and climate projections. Here, we combine surface height data from satellite radar altimeters with satellite-derived ice velocities and a new model of firn-layer evolution to generate a high-resolution map of time-averaged (2010–2018) basal melt rates and time series (1994–2018) of meltwater fluxes for most ice shelves. Total basal meltwater flux in 1994 (1,090 $\pm$ 150 Gt yr⁻¹) was similar to the steady-state value (1,100 $\pm$ 60 Gt yr⁻¹), but increased to 1,570 $\pm$ 140 Gt yr⁻¹ in 2009, followed by a decline to 1,160 $\pm$ 150 Gt yr⁻¹ in 2018. For the four largest 'cold-water' ice shelves, we partition meltwater fluxes into deep and shallow sources to reveal distinct signatures of temporal variability, providing insights into climate forcing of basal melting and the impact of this melting on the Southern Ocean.

The mass budget of the Antarctic ice sheet is controlled primarily by mass gain from net snow accumulation and mass loss from basal melting and iceberg calving of its floating ice shelves. These mass-loss processes act to maintain the ice shelf in steady state; however, many ice shelves are experiencing net mass loss[1] and thinning[2] due to ocean-driven basal melting in excess of the steady-state values. Confined ice shelves reduce the speed of grounded ice flowing into them by exerting back stress from sidewall friction and basal pinning points, a process called 'buttressing'[3]. Excess basal melting in recent decades has reduced buttressing and increased dynamic mass loss of grounded ice, which has increased Antarctica's contribution to sea level rise[4,5].

Ice-shelf melting has been categorized into three modes corresponding to distinct oceanographic processes[6]. Mode 1 melting occurs at the deep grounding lines of 'cold-water' ice shelves and is driven by inflows of cold, dense high salinity shelf water (HSSW) that is produced through sea ice formation on the continental shelf[7]. Rising plumes of buoyant and potentially supercooled meltwater (referred to as ice shelf water; ISW) formed from Mode 1 melting can lead to refreezing downstream, creating a layer of marine ice on the ice-shelf base[8]. Mode 2 melting occurs at 'warm-water' ice shelves where a subsurface layer of warm circumpolar deep water (CDW) or modified CDW (mCDW) is transported into the ice-shelf cavity. Mode 3 melting occurs near the ice front where seasonally warmed Antarctic surface water (AASW) can be transported under shallow ice by tides and other ocean variability. The relative contributions of these modes to total melting are highly variable around Antarctica, both in space and time, since each mode is influenced by several external processes, including regional atmospheric and oceanic conditions and the production and transport of sea ice[9,10].

The changing net fluxes and distribution of freshwater from ice-shelf basal melting influence other components of the climate system through processes such as the production and extent of sea ice, which modifies the exchange of heat, freshwater and gases (for example, carbon dioxide) between the atmosphere and Southern Ocean[11,12]; formation of Antarctic bottom water (AABW) that is a major driver of the global ocean overturning circulation[13]; and generation of nearshore coastal currents that advect freshwater and other tracers to connect different regions around Antarctica[14,15]. Despite the projected impacts of changes in ice-shelf melting on Southern Ocean dynamics and global climate variability[16], the current generation of global climate models such as those used in the Coupled Model Intercomparison Project[17] does not include realistic representations of meltwater fluxes[18].

Satellite-derived estimates of basal melt rates

Currently, the best available circum-Antarctic datasets for ice-shelf basal melt rates are derived from Ice, Cloud and Land Elevation Satellite (ICESat) laser altimetry acquired during 2003–2008[19,20]. These estimates are 6-yr averages for the satellite's operational period, with no information about temporal variability. Although ICESat's orbit to 86° S sampled all Antarctic ice shelves, it had relatively wide cross-track spacing, particularly for the northerly ice shelves (Supplementary Fig. 1). Existing data therefore cannot capture critical properties of meltwater fluxes from ice shelves, such as small spatial scales of melting in channels[21,22] or the large decadal variability inferred from oceanographic observations in West Antarctica[4].

A sequence of four European Space Agency satellite missions carrying radar altimeters have continuously acquired ranging data that allow us to estimate surface height change over Antarctica's ice shelves from 1994 to 2018: ERS-1, ERS-2, and Envisat (1992–2010) to 81.5° S and CryoSat-2 (2010–) to 88° S. CryoSat-2 samples nearly all ice shelf areas. Its orbit provides much higher track density than the earlier altimeters (Supplementary Fig. 1), which, together with its innovative synthetic aperture radar-interferometric mode of

[1]Scripps Institution of Oceanography, University of California San Diego, La Jolla, CA, USA. [2]Cryospheric Science Laboratory, NASA Goddard Space Flight Center, Greenbelt, MD, USA. [3]Earth and Space Research, Corvallis, OR, USA. [4]Department of Geophysics, Colorado School of Mines, Golden, CO, USA. ✉e-mail: suadusum@ucsd.edu
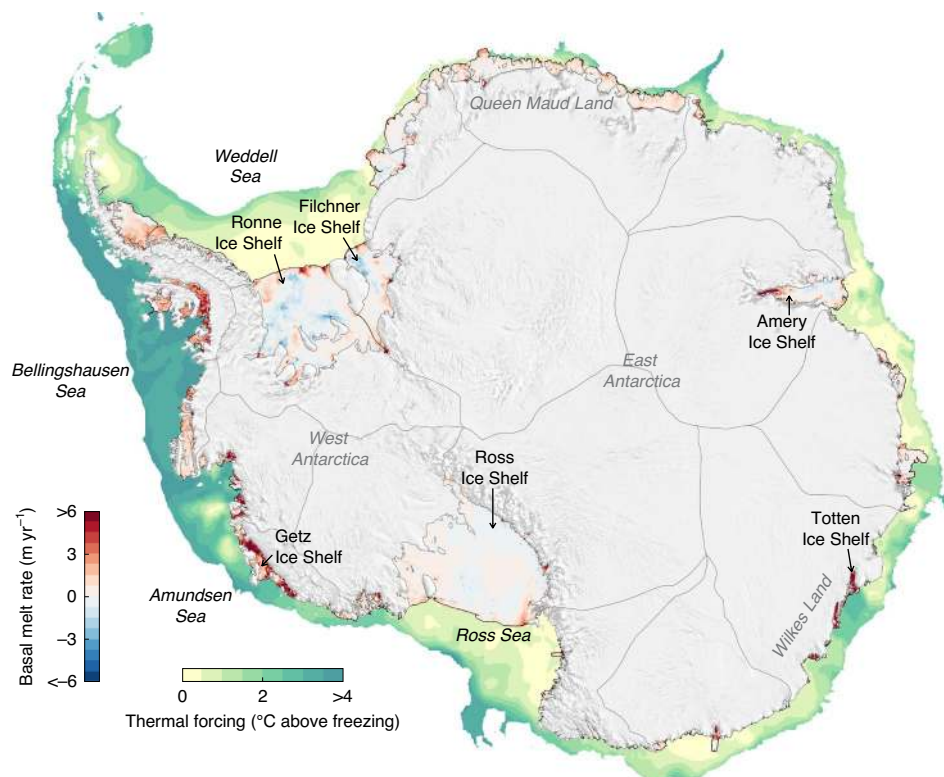
Fig. 1 | Basal melt rates of Antarctic ice shelves estimated using CryoSat-2 altimetry. Rates are averaged over 2010–2018. The units are m of ice equivalent per year, assuming an ice density of 917 kg m^{-3}. The thermal forcing, defined as the temperature above the in situ freezing point of seawater, is mapped for water depths <1,500 m. For water depths less than 200 m, the seafloor thermal forcing is shown, and for water depths >200 m, the maximum thermal forcing between 200 m and 800 m is shown (Methods).

operation[23], allows us to estimate height changes with higher spatial resolution and accuracy[22]. Here, we estimated time-averaged (over eight years, 2010–2018) basal melt rates on a high spatial resolution grid (500 m cells) for all ice shelves where sufficient data are available by combining height changes from CryoSat-2 radar altimetry with satellite-derived ice velocities and a new model of surface mass balance and firn state variability (Methods). We then used the continuous height record from the four altimetry missions to estimate basal melt rates in 10-km grid cells for every year from 1994 to 2018 for all Antarctic ice-shelf regions where sufficient data are available.

Spatial distribution of basal melt rates

The spatial distribution of time-averaged ice-shelf melt rates around Antarctica during 2010–2018 (Fig. 1) shows large differences between cold- and warm-water ice shelves. Cold-water ice shelves (such as Ross, Ronne, Filchner and Amery) show high melt rates under deep ice drafts near grounding lines and shallower ice drafts near ice fronts (Fig. 1, ice draft shown in Supplementary Fig. 2) separated by zones of refreezing. Warm-water ice shelves such as those in the Amundsen and Bellingshausen seas typically have high melt rates, consistent with the higher values of thermal forcing (temperature above the pressure-dependent, in situ freezing point of seawater) found near their ice fronts.

Area-integrated meltwater fluxes binned by ice draft for four cold-water and two warm-water ice shelves (Fig. 2) provide further insight into the different modes of melting occurring at different locations. Melting for regions of deep ice draft under the large cold-water ice shelves is dominated by Mode 1 processes. In steady state, refreezing rates can be high, and about half of all Mode 1 meltwater produced under Ronne Ice Shelf and about a fifth of all meltwater produced under Amery Ice Shelf is subsequently refrozen

as marine ice. The predicted thickness of marine ice estimated from our refreezing rates for Ronne and Amery ice shelves agrees well with independent estimates from airborne radar sounding and satellite radar altimetry (Supplementary Fig. 3). Refreezing typically starts at ice drafts that are around 50% of the grounding line depth, consistent with predictions from idealized models that use buoyant plume theory[24,25]. The ranges of ice draft for regions with refreezing (Fig. 2) also correspond with the approximate depths for the subsurface plumes of cold ISW found along ice fronts[26–28], which subsequently contribute to the formation of AABW[29].

Cold-water ice shelves also have regions of relatively high basal melt rates under shallower ice drafts along the ice fronts (Figs. 1 and 2), due primarily to Mode 3 melting. Unlike regions undergoing Mode 1 melting that are close to the deep grounding lines where ice-shelf thinning could substantially reduce buttressing[30,31], regions of Mode 3 melting are typically within the 'passive ice zones'[32] that provide little buttressing to grounded ice. However, the elevated melt rates contribute to increased ocean stratification along the ice front that influences cross-front exchanges of ocean heat[33] and the seasonal cycle of sea-ice formation close to the ice front[34], both of which feed back into the seasonal cycle of ice-shelf melt rates[35,36].

Under warm-water ice shelves, high melt rates are associated with subsurface flows of CDW and mCDW (Mode 2 melting). Melting in excess of steady state caused rapid thinning of several warm-water ice shelves in the Amundsen and Bellingshausen seas sectors during 2010–2018 (Supplementary Fig. 4). For some ice shelves in these sectors (for example, George VI, Wilkins and Dotson), the highest rates of thinning occurred in narrow basal channels. Getz Ice Shelf, the largest single source of meltwater from the Antarctic ice shelves (Supplementary Table 1), shows excess melting at depths between 250 m and 700 m (Fig. 2). Warm-water ice shelves outside the
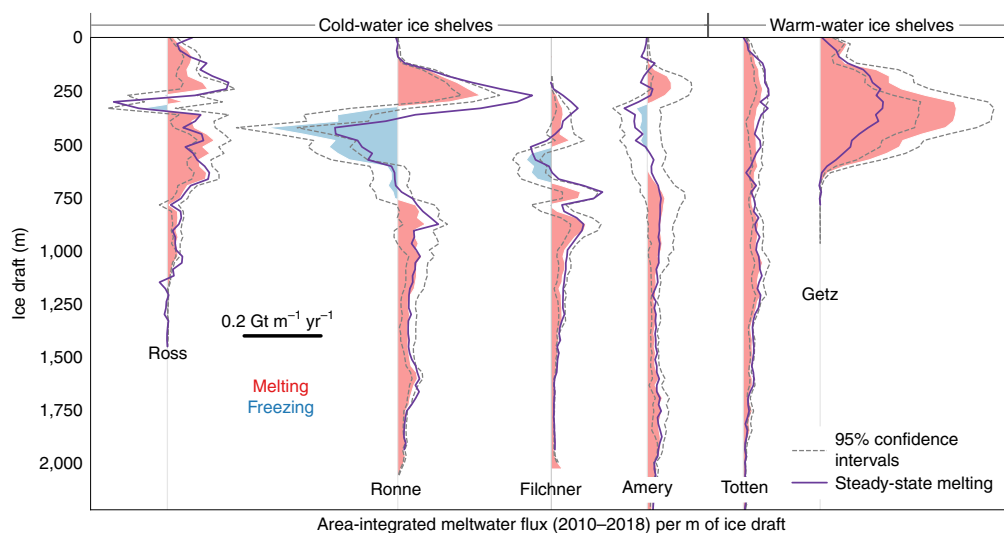
Fig. 2 | Vertical structure of melting and refreezing rates for selected ice shelves. Depth dependence of area-integrated meltwater flux (2010–2018) per m of ice-shelf draft (depth of the ice-shelf base below sea level) for six ice shelves (locations shown in Fig. 1). The scale for the horizontal axis is shown by the solid black line within the figure. The shaded regions in red and blue represent the mean values, and the dashed lines represent 95% confidence intervals. The purple lines are hypothetical steady-state meltwater fluxes (that is, the meltwater fluxes required to maintain constant ice-shelf mass). Warm-water ice shelves are distinguished from cold-water ice shelves by their higher average rates of meltwater production driven by intrusions of warm CDW or mCDW into the ice-shelf cavity.

Amundsen and Bellingshausen seas sector, such as Totten Ice Shelf in East Antarctica, do not show substantial rates of excess melting.

Variations in ice-shelf melt rates between 1994 and 2018

Our estimate for net mass loss due to thinning of Antarctic ice shelves from 1994 to 2018 is 3,960 ± 1,100 Gt (Fig. 3a; error range is the 95% confidence interval). Most of this mass loss was from the Pacific Ocean Sector ice shelves. For reference, the net loss of grounded ice from the Antarctic Ice Sheet during 1992–2017 was 2,660 ± 560 Gt[37]. The total meltwater flux, based on the area-integrated basal melt rate over all Antarctic ice shelves averaged over 1994–2018, was 1,260 ± 150 Gt yr^{-1}, which was 160 ± 150 Gt yr^{-1} higher than the steady-state rate of 1,100 ± 60 Gt yr^{-1} (Fig. 3b). Meltwater fluxes varied substantially with time: an increase of 480 ± 210 Gt yr^{-1}, from 1,090 ± 150 Gt yr^{-1} at the start of the record in 1994 to 1,570 ± 140 Gt yr^{-1} in 2009, was offset by a subsequent decrease of 410 ± 210 Gt yr^{-1} to 1,160 ± 150 Gt yr^{-1} in 2018. Our estimate of time-averaged meltwater flux for the ICESat-era (2003–2008) is 1,500 ± 140 Gt yr^{-1}, which is consistent with two previous ICESat-based estimates of 1,500 ± 240 Gt yr^{-1} (ref. [19]) and 1,450 ± 170 Gt yr^{-1} (ref. [20]). The ICESat-era estimate of meltwater flux exceeds our 25-yr average by 240 ± 210 Gt yr^{-1} and exceeds our steady-state estimate by 400 ± 160 Gt yr^{-1}, highlighting the importance of long, continuous records to provide context to results from individual missions[1] or between two non-overlapping missions[38].

We examined the temporal variability in melt rates from different modes of melting for the four largest cold-water ice shelves by calculating spatial averages over select regions (Fig. 4a–d) of deep ice draft (Mode 1) and shallow draft (mostly Mode 3). For Ross Ice Shelf, the timing of the minimum in Mode 1 melt rates in Byrd Inlet near 2015 is consistent with the 2013–2014 minimum in HSSW salinity on the Ross Sea continental shelf[39] and the timescale for advection of HSSW to Byrd Glacier[36]. The lower salinity for HSSW reduces the negative buoyancy driving HSSW under the ice front and downslope to the deep grounding line of Byrd Glacier, weakening the circulation of HSSW into Byrd Inlet and the resulting melting. Mode 1 melting of Filchner and Ronne ice shelves has been hypothesized to have increased following the formation of an

anomalously large polynya during the 1997–1998 austral summer[40]. This hypothesis was based on a sharp decline in ocean temperatures at an instrumented site (Site 5; Supplementary Fig. 5) on Ronne Ice Shelf near the southwestern Berkner Island coast between 2000 and 2003, attributed[40] to increased ISW formation following a period of high Mode 1 melting. Our data support this hypothesis, with increased melt rates at deep ice drafts under Filchner Ice Shelf during 1999–2000 and decreased melt rates (including a short-lived transition to refreezing) at Site 5 between 2000 and 2004 (Supplementary Fig. 5). Melt rates of Amery Ice Shelf, spatially averaged for deep ice drafts, varied from near 0 to 6.5 m yr^{-1}, with a maximum value between 2003 and 2007. We speculate that this maximum could be associated with a continuous drainage of a ~0.8 km^3 subglacial lake under Lambert Glacier between 2003 and 2006[41]; subglacial discharge is known to drive energetic plumes[42,43] that increase basal melt rates near grounding lines.

For Amundsen Sea ice shelves, melt rates showed substantial variability, with the highest sustained melt rates occurring in the late 2000s (Fig. 4e). Variability in Mode 2 melting of Amundsen Sea ice shelves has been previously identified in ocean observations and linked to variability in the tropical Pacific at both interannual[44,45] and decadal[4] timescales. The magnitude of variability in our estimated melt rates of Dotson Ice Shelf (around 60 Gt yr^{-1} peak to trough) is consistent with the variability in independent estimates of meltwater flux from repeated oceanographic sections along the ice-shelf front[4] (Supplementary Fig. 6) but is larger than the variability expected from an ocean model that used atmospheric forcing from the same period[46]. Excess basal melting and changes in ice-shelf extent (Supplementary Fig. 8 and Supplementary Table 1) in the Amundsen Sea sector between 1994 and 2018 could be due to a longer-term increase in the thickness of CDW incursions under ice-shelf cavities associated with atmospheric and oceanic responses to anthropogenic forcing[47].

Our new estimates of time-varying melt rates allows assessment of whether ocean circulation models are adequately representing the complex feedbacks between water-mass production and conversion processes acting under the ice shelves and over the continental shelves offshore. The temporal variability of
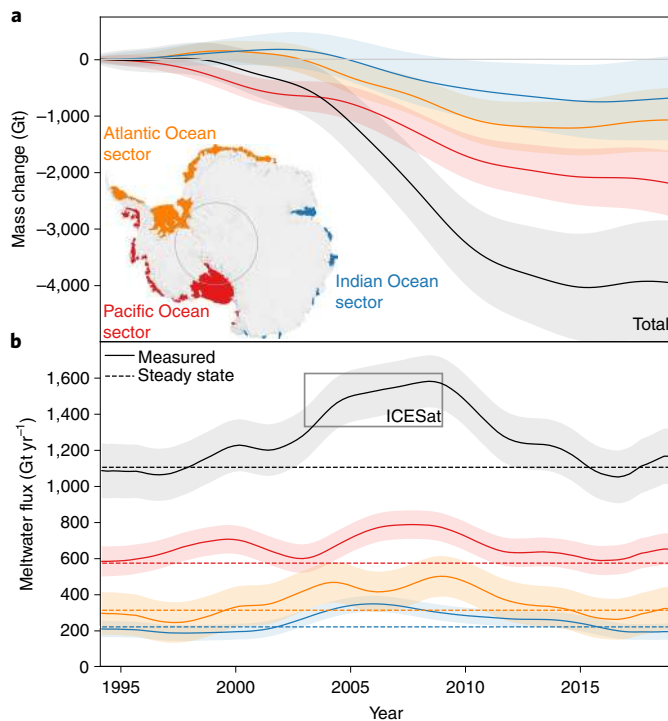
Fig. 3 | Variations in Antarctic ice-shelf mass between 1994 and 2018.
a, Cumulative ice-shelf mass change between 1994 and 2018 for the Pacific (red), Atlantic (orange), and Indian (blue) ocean sectors of Antarctica, with shading showing 95% confidence intervals. The region definitions are shown on the inset map, and the combined total for all ice shelves is shown in black. **b**, Meltwater fluxes for 1994–2018 from ocean-driven ice-shelf basal melting for the same regions. Dashed lines represent meltwater fluxes in steady state, where the mass of the ice shelves is constant through time. Total meltwater flux estimates for the ICESat era (grey box) are averaged between two studies[19,20] (width indicates time period, height indicates 95% confidence interval).

Fig. 4 | Time-dependent basal melt rates for different modes of melting.
a–**d**, Area-averaged basal melt rates (in m of ice equivalent per year) for selected regions within the four largest Antarctic ice shelves. **a**, Ross. **b**, Ronne. **c**, Filchner. **d**, Amery. Regions shown in red experience melting predominantly from cold HSSW inflows at deep ice drafts (Mode 1), while regions shown in blue typically experience melting from intrusions of AASW at shallow ice drafts (Mode 3). **e**, Basal melt rates for Amundsen Sea ice shelves, which experience melting from inflows of warm CDW (Mode 2). Gaps in the spatial coverage reflect the sampling of the altimeters before CryoSat-2.

melting in all three modes (Fig. 4) will contribute to changes in the distribution of different water masses over the Antarctic continental shelf seas and into the global ocean. The ISW produced through Mode 1 melting contributes to the formation of particularly cold, dense forms of AABW[26,48,49]. Changes in Mode 2 and Mode 3 melting modify the fluxes of meltwater into the upper ocean in adjacent coastal regions[15,34]. Increased ocean stratification from shallow sources of cold, buoyant water alters the seasonal cycle of sea ice[50] and decreases the potential for deep convection that drives production of dense shelf-water types including HSSW. Changes in relative strengths of these melt modes modify the geostrophic ocean circulation over the Antarctic continental shelf seas, feeding back into the transport of ocean heat between coastal sectors and into the sub-ice-shelf cavities[7].

We have produced two new datasets of basal melt rates for nearly all of Antarctica's ice shelves. One dataset provides melt rates at high spatial resolution (500 m grid) for most ice-shelf areas, averaged over the period 2010–2018. The second dataset allows for the evaluation of annual estimates of basal melt rates at lower spatial resolution (>10 km) for the period 1994–2018. Together, these datasets reveal large variability in total meltwater fluxes from individual Antarctic ice shelves, with distinct, regionally variable, signatures of temporal variability for different modes of ocean-driven melting. Our data provide insights into the glaciological and climate drivers of processes that modulate current ice-sheet mass loss, and
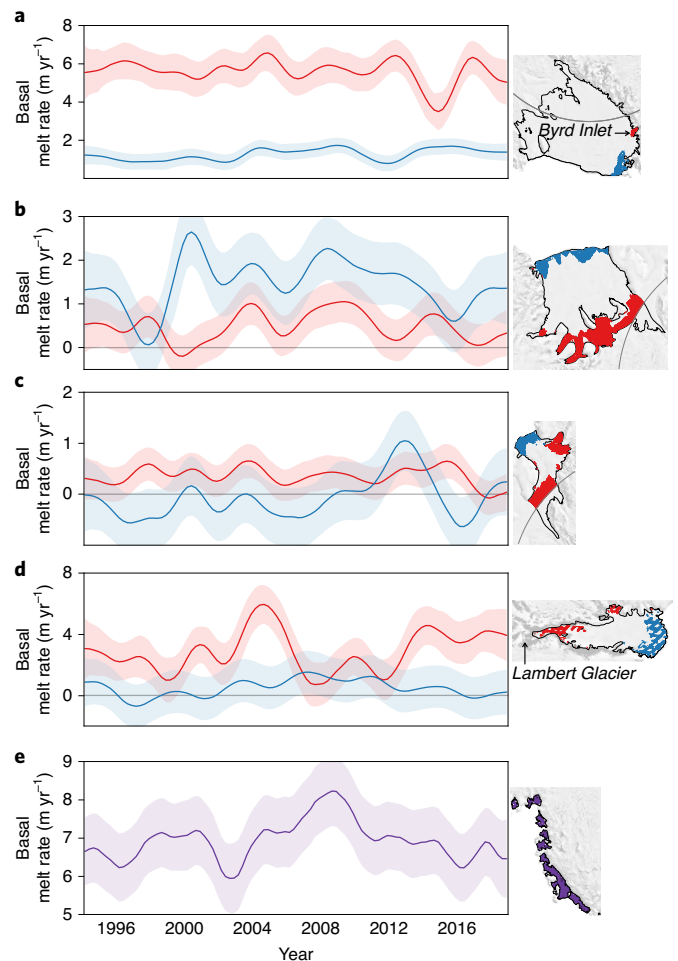
improved metrics for calibration and validation of melt rates used in both ice–ocean and Earth-system models.

Online content

Any methods, additional references, Nature Research reporting summaries, source data, extended data, supplementary information, acknowledgements, peer review information; details of author contributions and competing interests; and statements of data and code availability are available at https://doi.org/10.1038/s41561-020-0616-z.

References

1. Pritchard, H. D. et al. Antarctic ice-sheet loss driven by basal melting of ice shelves. *Nature* **484**, 502–505 (2012).
2. Paolo, F. S., Fricker, H. A. & Padman, L. Volume loss from Antarctic ice shelves is accelerating. *Science* **348**, 327–331 (2015).

3. Thomas, R. H., Sanderson, T. J. O. & Rose, K. E. Effect of climatic warming on the West Antarctic ice sheet. *Nature* **277**, 355–358 (1979).
4. Jenkins, A. et al. West Antarctic ice sheet retreat in the Amundsen Sea driven by decadal oceanic variability. *Nat. Geosci.* **11**, 733–738 (2018).
5. Nerem, R. S. et al. Climate-change–driven accelerated sea-level rise detected in the altimeter era. *Proc. Natl Acad. Sci. USA* **115**, 2022–2025 (2018).
6. Jacobs, S. S., Helmer, H. H., Doake, C. S. M., Jenkins, A. & Frolich, R. M. Melting of ice shelves and the mass balance of Antarctica. *J. Glaciol.* **38**, 375–387 (1992).
7. Nicholls, K. W. Predicted reduction in basal melt rates of an Antarctic ice shelf in a warmer climate. *Nature* **388**, 460–462 (1997).
8. Lewis, E. L. & Perkin, R. G. Ice pumps and their rates. *J. Geophys. Res. Oceans* **91**, 11756–11762 (1986).
9. Turner, J. et al. Atmosphere-ocean-ice interactions in the Amundsen Sea Embayment, West Antarctica. *Rev. Geophys.* **55**, 235–276 (2017).
10. Rintoul, S. R. The global influence of localized dynamics in the Southern Ocean. *Nature* **558**, 209–218 (2018).
11. Pauling, A. G., Smith, I. J., Langhorne, P. J. & Bitz, C. M. Time-dependent freshwater input from ice shelves: impacts on Antarctic sea ice and the Southern Ocean in an Earth system model. *Geophys. Res. Lett.* **44**, 10454–10461 (2017).
12. Merino, N. et al. Impact of increasing Antarctic glacial freshwater release on regional sea-ice cover in the Southern Ocean. *Ocean Model.* **121**, 76–89 (2018).
13. Fogwill, C. J., Phipps, S. J., Turney, C. S. M. & Golledge, N. R. Sensitivity of the Southern Ocean to enhanced regional Antarctic ice sheet meltwater input. *Earths Future* **3**, 317–329 (2015).
14. Moffat, C., Beardsley, R. C., Owens, B. & van Lipzig, N. A first description of the Antarctic Peninsula Coastal Current. *Deep Sea Res. Part II* **55**, 277–293 (2008).
15. Nakayama, Y., Timmermann, R., Rodehacke, C. B., Schröder, M. & Hellmer, H. H. Modeling the spreading of glacial meltwater from the Amundsen and Bellingshausen Seas. *Geophys. Res. Lett.* **41**, 7942–7949 (2014).
16. Golledge, N. R. et al. Global environmental consequences of twenty-first-century ice-sheet melt. *Nature* **566**, 65–72 (2019).
17. Eyring, V. et al. Overview of the Coupled Model Intercomparison Project Phase 6 (CMIP6) experimental design and organization. *Geosci. Model Dev.* **9**, 1937–1958 (2016).
18. Jourdain, N. C. et al. A protocol for calculating basal melt rates in the ISMIP6 Antarctic ice sheet projections. Preprint at https://doi.org/10.5194/tc-2019-277 (2019).
19. Rignot, E., Jacobs, S., Mouginot, J. & Scheuchl, B. Ice-shelf melting around Antarctica. *Science* **341**, 266–270 (2013).
20. Depoorter, M. A. et al. Calving fluxes and basal melt rates of Antarctic ice shelves. *Nature* **502**, 89–92 (2013).
21. Dutrieux, P. et al. Pine Island glacier ice shelf melt distributed at kilometre scales. *Cryosphere* **7**, 1543–1555 (2013).
22. Gourmelen, N. et al. Channelized melting drives thinning under a rapidly melting Antarctic ice shelf. *Geophys. Res. Lett.* **44**, 9796–9804 (2017).
23. Wingham, D. J. et al. CryoSat: A mission to determine the fluctuations in Earth's land and marine ice fields. *Advances in Space Research* **37**, 841–871 (2006).
24. Lane-Serff, G. F. On meltwater under ice shelves. *J. Geophys. Res. Oceans* **100**, 6961–6965 (1995).
25. Holland, P. R., Feltham, D. L. & Jenkins, A. Ice shelf water plume flow beneath Filchner-Ronne Ice Shelf, Antarctica. *J. Geophys. Res. Oceans* **112**, C05044 (2007).
26. Foldvik, A. Ice shelf water overflow and bottom water formation in the southern Weddell Sea. *J. Geophys. Res.* **109**, C02015 (2004).
27. Smethie, W. M. & Jacobs, S. S. Circulation and melting under the Ross Ice Shelf: estimates from evolving CFC, salinity and temperature fields in the Ross Sea. *Deep Sea Res. Part I* **52**, 959–978 (2005).
28. Herraiz-Borreguero, L., Lannuzel, D., Merwe, P., van der, Treverrow, A. & Pedro, J. B. Large flux of iron from the Amery Ice Shelf marine ice to Prydz Bay, East Antarctica. *J. Geophys. Res. Oceans* **121**, 6009–6020 (2016).
29. Schlosser, P. et al. Oxygen 18 and helium as tracers of ice shelf water and water/ice interaction in the Weddell Sea. *J. Geophys. Res.* **95**, 3253–2363 (1990).
30. Reese, R., Gudmundsson, G. H., Levermann, A. & Winkelmann, R. The far reach of ice-shelf thinning in Antarctica. *Nat. Clim. Change* **8**, 53–57 (2018).
31. Goldberg, D. N., Gourmelen, N., Kimura, S., Millan, R. & Snow, K. How accurately should we model ice shelf melt rates? *Geophys. Res. Lett.* **46**, 189–199 (2019).
32. Fürst, J. J. et al. The safety band of Antarctic ice shelves. *Nat. Clim. Change* **6**, 479–482 (2016).
33. Malyarenko, A., Robinson, N. J., Williams, M. J. M. & Langhorne, P. J. A wedge mechanism for summer surface water inflow into the Ross Ice Shelf cavity. *J. Geophys. Res. Oceans* **124**, 1196–1214 (2019).
34. Porter, D. F. et al. Evolution of the seasonal surface mixed layer of the Ross Sea, Antarctica, observed with autonomous profiling floats. *J. Geophys. Res. Oceans* **124**, 4934–4953 (2019).
35. Stewart, C. L., Christoffersen, P., Nicholls, K. W., Williams, M. J. M. & Dowdeswell, J. A. Basal melting of Ross Ice Shelf from solar heat absorption in an ice-front polynya. *Nat. Geosci.* **12**, 435–440 (2019).
36. Tinto, K. J. et al. Ross Ice Shelf response to climate driven by the tectonic imprint on seafloor bathymetry. *Nat. Geosci.* **12**, 441–449 (2019).
37. The IMBIE team Mass balance of the Antarctic Ice Sheet from 1992 to 2017. *Nature* **558**, 219–222 (2018).
38. Smith, B. E. et al. Pervasive ice sheet mass loss reflects competing ocean and atmosphere processes. *Science* **368**, 1239–1242 (2020).
39. Castagno, P. et al. Rebound of shelf water salinity in the Ross Sea. *Nat. Commun.* **10**, 5441 (2019).
40. Nicholls, K. W. & Østerhus, S. Interannual variability and ventilation timescales in the ocean cavity beneath Filchner-Ronne Ice Shelf, Antarctica. *J. Geophys. Res. Oceans* **109**, C04014 (2004).
41. Smith, B. E., Fricker, H. A., Joughin, I. R. & Tulaczyk, S. An inventory of active subglacial lakes in Antarctica detected by ICESat (2003–2008). *J. Glaciol.* **55**, 573–595 (2009).
42. Motyka, R. J., Dryer, W. P., Amundson, J., Truffer, M. & Fahnestock, M. Rapid submarine melting driven by subglacial discharge, LeConte Glacier, Alaska. *Geophys. Res. Lett.* **40**, 5153–5158 (2013).
43. Washam, P., Nicholls, K. W., Münchow, A. & Padman, L. Summer surface melt thins Petermann Gletscher Ice Shelf by enhancing channelized basal melt. *J. Glaciol.* **65**, 662–674 (2019).
44. Dutrieux, P. et al. Strong sensitivity of Pine Island Ice-Shelf melting to climatic variability. *Science* **343**, 174–178 (2014).
45. Paolo, F. S. et al. Response of Pacific-sector Antarctic ice shelves to the El Niño/Southern Oscillation. *Nat. Geosci.* **11**, 121–126 (2018).
46. Kimura, S. et al. Oceanographic controls on the variability of ice-shelf basal melting and circulation of glacial meltwater in the Amundsen Sea Embayment, Antarctica. *J. Geophys. Res. Oceans* **122**, 10131–10155 (2017).
47. Holland, P. R., Bracegirdle, T. J., Dutrieux, P., Jenkins, A. & Steig, E. J. West Antarctic ice loss influenced by internal climate variability and anthropogenic forcing. *Nat. Geosci.* **12**, 718–724 (2019).
48. Budillon, G., Castagno, P., Aliani, S., Spezie, G. & Padman, L. Thermohaline variability and Antarctic bottom water formation at the Ross Sea shelf break. *Deep Sea Res. Part I* **58**, 1002–1018 (2011).
49. Williams, G. D. et al. The suppression of Antarctic bottom water formation by melting ice shelves in Prydz Bay. *Nat. Commun.* **7**, 12577 (2016).
50. Petty, A. A., Holland, P. R. & Feltham, D. L. Sea ice and the ocean mixed layer over the Antarctic Shelf seas. *Cryosphere* **8**, 761–783 (2014).

Methods

Melt rates from Lagrangian CryoSat-2 analysis, 2010–2018. In a Lagrangian reference frame (following a parcel of ice), and assuming that the ice shelf is floating in hydrostatic balance, the net ice-shelf height change (Dh/Dt) observed using satellite altimetry, where h is the ice-shelf surface height relative to the height of the ocean surface h_{ocean}, is related to the surface mass balance (M_s; kg m^{-2} yr^{-1}), basal melt rate (w_b; m of ice equivalent per year), ice shelf divergence ($H_i \nabla \cdot \mathbf{v}$; in m of ice equivalent per year) and changes in firn air content (h_{air}; m) through[51]:

$$\frac{Dh}{Dt} = \frac{(\rho_w - \rho_i)}{\rho_w}\left(\frac{M_s}{\rho_i} - H_i \nabla \cdot \mathbf{v} - w_b\right) + \frac{Dh_{air}}{Dt}, \qquad (1)$$

where $\mathbf{v}$ is the two-dimensional grid of ice surface velocity vectors (m yr^{-1}), H_i is ice-shelf thickness in units of m of ice equivalent, ρ_w is the density of ocean water (assumed to be 1,028 kg m^{-3}) and ρ_i is the density of ice (assumed to be 917 kg m^{-3}). Here, H_i is given by $H_i = H - h_{air}$, where H is the total ice-shelf thickness (surface to base). In the following four sections, we describe the various datasets used in our estimation of w_b through Equation (1).

Height of the ocean surface. We estimated the height of ocean surface h_{ocean} as:

$$h_{ocean} = h_{geoid} + h_{mdt} + h_{ot} + h_{ibe} + h_{lt} + h_{slr}, \qquad (2)$$

where h_{geoid} is the height of the EIGEN-6C4 geoid[52], h_{mdt} is mean dynamic topography from DTU13MDT[53], h_{ot} is the ocean tide from the CATS2008 tide model[54] (an update to the model described by ref. [55]), h_{ibe} is a correction for the inverse barometer effect due to atmospheric pressure variability and is obtained from the MOG2D dynamic atmosphere correction[56], h_{lt} is the ocean load tide estimated using the TPXO7.2 model[57], and h_{slr} is the increase in mean sea level around the Antarctic coast reported by ref. [58]. Of the terms on the right-hand side of Equation (2), we only considered temporal variability of h_{ot}, h_{ibe}, h_{lt}, and h_{slr}.

Lagrangian height changes. We derived Dh/Dt, following ref. [51], by first advecting the locations of CryoSat-2 footprints, initially at $\mathbf{x}_{t_0}$, to their 2015 locations $\mathbf{x}$ using:

$$\mathbf{x} = \mathbf{x}_{t_0} + \sum_{t_0}^{2015} \mathbf{v}_{2015}\Delta t, \qquad (3)$$

where Δt is 0.01 years. For $\mathbf{v}_{2015}$, we used ice velocities from a 2015 mosaic derived from Landsat-8 feature tracking at 300 m posting[59]. For the ice shelves where the southern limit of these velocity data (82.4° S) did not include the entire area (Filchner, Ronne and Ross), we filled in data gaps in the 2015 mosaic using 1996–2016 mean values from ref. [60]. The velocity data were adjusted to reflect velocities in the Antarctic polar stereographic projection with a standard parallel of 71° and a standard longitude of 0°. We converted latitudes and longitudes of CryoSat-2 data into $\mathbf{x}$ using the same projection. Using the advected CryoSat-2 data, we estimated Dh/Dt and associated uncertainties in grid cells at 500 m spacing and 1 km resolution using the 'plane fit' technique described by ref. [61] (their section S1). We discarded data in a grid cell when the uncertainty in Dh/Dt estimated from the plane fit was greater than 0.5 m yr^{-1}.

Thickness change due to ice-shelf divergence ($H_i \nabla \cdot \mathbf{v}$). We estimated the $H_i \nabla \cdot \mathbf{v}$ term in Equation (1) using ice thickness (H_i) estimated from CryoSat-2 data following ref. [61] but using the advected footprint locations as described in Lagrangian height changes, above. For $\nabla \cdot \mathbf{v}$, we used strain rate estimates and associated uncertainties from ref. [62], based on velocity data collected between 2013 and 2016 north of 82.4° S. Over Filchner, Ronne and Ross ice shelves, these data did not extend to their southern limits. Therefore, we used values of $\nabla \cdot \mathbf{v}$ provided by ref. [51] for Filchner, Ronne and Ross ice shelves.

M_s and height changes from firn processes (dh_{air}/dt). For the M_s term, we used NASA's global Modern-Era Retrospective analysis for Research and Applications, Version 2 (MERRA-2)[63], which we combined with an offline high-resolution MERRA-2 'replay,' denoted M2R12K[38], to derive a hybrid product referred to as 'MERRA-2 Hybrid.' M2R12K is a high-resolution MERRA-2 run (12.5 km) specifically targeted over the Antarctic and spanning 2000–2014. To maintain the fine spatial resolution of the M2R12K, its mean seasonal cycle is combined with the seasonal residuals from the full MERRA-2 period (1980–2019). Thus, MERRA-2 Hybrid combines the fine spatial resolution from M2R12K with the longer time record from MERRA-2. We used MERRA-2 Hybrid forcings (precipitation minus evaporation, skin temperature and meltwater flux from a degree-day model) for simulations of the firn column using the densification equations described in ref. [64] implemented in the Community Firn Model[65] to estimate dh_{air}/dt[38]. We refer to this firn densification model as GSFC-FDMv0, which is calibrated with ~200 firn depth-density profiles from both the Greenland and Antarctic ice sheets and includes both dry and wet firn processes. We assume that $Dh_{air}/Dt = dh_{air}/dt$ because of the low spatial resolution of the firn model output compared with the distances over which the CryoSat-2 footprints were advected in the Lagrangian framework. GSFC-FDMv0 provides dh_{air}/dt values at 12.5 km spatial posting and five day temporal sampling[38]. We interpolated these data in space to the grid cells at 500 m spacing used to derive Dh/Dt. Details regarding GSFC-FDMv0 are within the supplementary materials of ref. [38].

Steady-state basal melt rates. We estimated the 'steady-state' basal melt rate, $w_{b,steady}$, required to keep ice shelves in steady-state mass balance (equivalent to assuming that there is no net change in H_i) using:

$$w_{b,steady} = \frac{\langle M_s \rangle}{\rho_i} - \langle \nabla \cdot (H_i \mathbf{v}) \rangle, \qquad (4)$$

where $\langle \rangle$ represents the time-average value. There is no temporal variability in our estimates of $w_{b,steady}$: we used the 1994–2018 mean values from the MERRA-2 Hybrid (precipitation minus evaporation: $P - E$) for M_s and assumed that outside the Amundsen Sea sector there was no change in $\nabla \cdot (H_i \mathbf{v})$ in time during our observation period.

Depth dependence of area-integrated meltwater fluxes. We estimated the ice-shelf draft, D_i, the depth of the ice-shelf base below mean sea level, using $D_i = \rho_i H_i / \rho_w$. For grid cells in which we were not able to estimate H_i, we used values estimated using BedMachine[66] (Supplementary Fig. 2e). We then calculated area-integrated meltwater fluxes as a function of ice-shelf draft D_i (Fig. 2) by integrating w_b in discrete bins of D_i at 30 m spacing.

Ocean thermal forcing. We define thermal forcing, ΔT (Fig. 1), as the temperature above the in situ freezing point of seawater, T_f. We obtained profiles of ocean temperature (T) and salinity (S) from the World Ocean Database 2018[67], then estimated the values of $T_f = (T,P)$, where P is pressure, from the function described by ref. [68] and implemented in the Gibbs SeaWater Oceanographic Toolbox of TEOS-10[69]. We only used profiles that satisfied one of the following criteria: (1) profile extends to at least 800 m in water depth z_b deeper than 800 m or (2) profile extends to within 150 m of the seabed (evaluated from Rtopo2[70]) for $z_b < 800$ m. We then determined maximum thermal forcing as the maximum value of ΔT in the depth range 200–min(z_b, 800) m. The limit of 200 m is designed to exclude summer-warmed AASW and focus on deeper water masses on the continental shelf that have access to the cavities under ice shelves; that is, primarily Mode 1 and Mode 2 melting. For $z_b < 200$ m, we take the value of ΔT at the deepest point in the profile. The values of ΔT were then interpolated to a 25-km uniform polar stereographic grid, with standard latitude and longitude of 71° S, 0° E, using a bi-cubic distance weighting scheme, modified to increase weightings along isobath and lower weightings across isobaths, consistent with known strong barotropic control of circulation over Antarctica's continental shelves and along the shelf break[71,72].

Time series of height change from Eulerian ERS-1, ERS-2, Envisat and CryoSat-2 analysis. In addition to 2010–2018 mean values of w_b from Lagrangian analysis of CryoSat-2 data, we estimated time-varying melt rates derived using Eulerian analysis of height change derived from ERS-1, ERS-2, Envisat and CryoSat-2 altimetry. We used consistent 10 km grid cells at 1 km posting for all missions, and data were averaged in time to three-month intervals. To merge height change data from all four missions to produce a continuous time series spanning 1992–2018, we only considered grid cells where there were sufficient valid data from all four missions.

We obtained ERS-1, ERS-2 and Envisat height data ($h_{ERS/Env}$) from refs. [73,74]. We corrected $h_{ERS/Env}$ for change in the ocean surface h_{ocean} using Equation (2).

We first derived height changes for each mission separately. For each grid cell, we estimated height changes for each mission if there were at least 15 data points spanning at least 3 years using:

$$h_{ERS/Env} = h_0 + f(x,y) + m_6 t + m_7 s + m_8 b + m_9 f + h_r(t) \qquad (5)$$

where $f(x,y) = m_1 x + m_2 y + m_3 x^2 + m_4 y^2 + m_5 xy$ represents surface topography, t is time in decimal years, s is a satellite ascending/descending binary flag (0 or 1), b is backscatter and f is a binary mode flag that is only applied to data from ERS-1 or ERS-2 on the basis of whether the heights were from ocean-mode or ice-mode data. The parameters in Equation (4) (h_0, m_{1-10}) were estimated using a robust linear regression where outliers outside the min(3σ, 10 m) range were discarded in 10 iterations. We estimated standard errors of the regression for each of the parameters in Equation (5) and discarded grid cells with an error greater than 0.3 m yr^{-1} in m_6. The residuals in the linear regression $h_r(t)$ were binned in three-month intervals and contain any temporal signal that is not included in a linear trend as well as noise.

The height-change rate (dh/dt) estimate for an ice shelf for each individual mission was then:

$$\frac{dh}{dt} = m_6 + \frac{dh_r}{dt} \qquad (6)$$

We processed CryoSat-2 data using the Eulerian plane-fit technique described in ref. [61] (their section S1) after applying the same geophysical corrections used for ERS-1, ERS-2 and Envisat data.

To avoid biases from different spatial sampling, we discarded data from all grid cells that did not contain height change measurements from all four missions. For grid cells where sufficient data were available, we then merged the height-change time series from the four radar altimeters by ensuring that height-change rate during the time periods with overlapping data was equal to the average of the height-change rates estimated from each altimeter. Therefore, we imposed $dh/dt = (dh_{ERS-1}/dt + dh_{ERS-2}/dt)/2$ during 1995–1996, $dh/dt = (dh_{ERS-2}/dt + dh_{Env}/dt)/2$ during 2002–2003, and $dh/dt = (dh_{ERS-2}/dt + dh_{Env}/dt)/2$ during 2010–2011. In addition to a merged multi-mission dh/dt time series, we obtained a merged height-change time series $h(t)$ referenced to the height at $t = 1994$ by integrating dh/dt in time.

Influence of surface melting on radar-derived height changes. We found large decreases in radar-derived height changes between 1992 and 1994 across Antarctica. In some previous studies[2,75], data from this period were excluded due to this anomalous signal. Using surface-melt data from RACMO (regional atmospheric model)[76] and a positive degree-day model based on MERRA-2[38], we found that this change in radar-derived height change was primarily due to a large circum-Antarctic surface-melt event in December 1991. This melt event probably created a bright radar reflector, and its burial following subsequent snowfall was tracked by the radar altimeter, which caused a downward trend in estimated height. Due to the large effect of this event across several ice shelves around Antarctica, we excluded this period in our analysis.

For Ross Ice Shelf, we found large changes in height following anomalous surface-melt events during the austral summers of 1991–1992, 2002–2003, and 2015–2016. Two of these (1991–1992 and 2015–2016) were the largest surface-melt events over the ice shelf during the full 1980–2019 MERRA-2 period[77]. We accounted for the radar response following such events by estimating a time series of h_{air} using height changes measured over grounded ice adjacent to the floating ice shelf, following the methodology of ref. [51]. We derived height changes over grounded ice up to 100 km from the ice shelf boundary in grid cells at 5 km spacing using the plane-fit technique described by ref. [78]. Each grid cell had at least 15 data points spanning a time interval of at least 3 years. We discarded grid cells with an uncertainty in estimated dh/dt greater than 0.3 m/yr. Since there were too few data to apply a spatially variable correction over the ice shelf, we followed ref. [51] to use a single time series for the entire ice shelf.

Time series of melt rates. From the merged multi-mission Eulerian height-change rate time series $dh(t)/dt$ spanning 1994–2018, we derived time series of basal melt rate anomalies ($w_{b,anom}$, relative to the 2010–2018 mean) using:

$$w_{b,anom}(t) = \frac{M_{s,anom}}{\rho_i} - \frac{\rho_w}{\rho_w - \rho_i}\left(\frac{dh_{anom}}{dt} - \frac{dh_{air,anom}}{dt}\right) - \nabla \cdot (H_i \mathbf{v})_{anom} \quad (7)$$

where $M_{s,anom}$, dh_{anom}/dt and $dh_{air,anom}/dt$ are anomalies (relative to the 2010–2018 mean) in rates of altimeter-derived height change, firn-air content from GSFC-FDMv0 and MERRA-2 P-E data, respectively, smoothed to three-month timescales using a moving average filter. We only considered anomalies in $\nabla \cdot (H_i \mathbf{v})$ for the Amundsen Sea sector, for which we used time-variable estimates of $\mathbf{v}$ from ref. [79] for the 1994–2013 period and from ref. [80] for the 2014–2017 period. Gaps in the time series of $\nabla \cdot (H_i \mathbf{v})_{anom}$ were filled using linear interpolation. We produced time series of basal melt rates, $w_b(t)$, by adding high-resolution melt rates from CryoSat-2 analysis (Section S1) to the time series of melt rate anomalies $w_{b,anom}(t)$. We assume that there was no change in w_b in regions south of 81.5° S, the orbit limit of the ERS-1, ERS-2 and Envisat satellites.

Uncertainty estimation. We compared GSFC-FDMv0 estimates of dh_{air}/dt with previously published estimates from an atmospheric model (RACMO2.3p2[76]) and the associated firn densification model (IMAU-FDM[81]) between 1979 and 2016 (the time period available for RACMO and IMAU-FDM). Using this comparison, we derived an uncertainty estimate using the combination of (a) sensitivity tests to quantify uncertainties from the assumption of steady-state climate that is used to spin up a firn densification model[1] (Supplementary Fig. 7a) and (2) standard deviations of differences between GSFC-FDMv0 and IMAU-FDM estimates of dh_{air}/dt values during 1980–2016 at GSFC-FDMv0 grid cell locations (these values are shown in Supplementary Fig. 7b for annual timescales, but they are smaller for the longer timescales typically considered in this study). We assumed that these uncertainties were Gaussian and uncorrelated, and added them in quadrature.

We estimated uncertainties for all terms in Equation (5) as the uncertainties from the linear regression and propagated these to $h(t)$ in Equation (6). Uncertainties in $h_r(t)$ were estimated as the standard deviation of heights from the residuals of Equation (5) within each quarterly bin. Uncertainties in $H_i \nabla \cdot \mathbf{v}$ were provided by ref. [62], uncertainties in M_s were estimated using a moving standard deviation at annual timescales and the uncertainties in the advection of heights from Lagrangian processing were not considered; compared with previously described uncertainty sources, the three sources here represent a substantially smaller component of total uncertainty.

We propagated these uncertainties to the filtered time series of basal melt rate using a bootstrap approach. For each ice shelf (or in the case of the top four panels

of Fig. 4, for regions within large ice shelves), we applied a filter to the average $h(t)$ time series that included both a gradient and a smoothing operator to estimate dh/dt. The residuals from the filtered time series were resampled 100 times, and each sample was combined with Gaussian random noise from the error sources described previously. These samples were added back to dh/dt and integrated to produce 100 resampled time series $h_{samp}(t)$, which were used to produce 100 time series of dh_{samp}/dt. The standard deviation of dh_{samp}/dt provided the final uncertainty in dh/dt. We estimated uncertainties in melt rates in the eight sectors around Antarctica by summing the uncertainties from all ice shelves in each sector in quadrature (Supplementary Table 1).

Estimates of marine ice thickness. We estimated the thickness of marine ice (H_{ma}) under Ronne and Amery ice shelves from our steady-state basal melt rate estimates, $w_{b,steady}$, using[82]:

$$\frac{dH_{ma}}{ds} = \frac{w_{b,steady} - H_{ma}\nabla \cdot \mathbf{v}}{|\mathbf{v}|} \quad (8)$$

where $H_{ma} \geq 0$ and s represents the distance along a flowline. Here, we use $w_{b,steady}$ instead of the time-stamped estimate (w_b) because the value of H_{ma} is a function of the accumulation and strain rates of an ice shelf at decadal to centennial timescales. We generated flowlines for Ronne and Amery ice shelves and solved Equation (8) using $\Delta s = |\mathbf{v}|\Delta t$ with $\Delta t = 1$ yr, assuming $H_{ma} = 0$ at the beginning of the flowline. Our estimated values of H_{ma} for both ice shelves show good agreement with independent estimates derived by differencing thicknesses derived from satellite altimetry and from radar sounding[83,84] (Supplementary Fig. 3).

Changes in iceberg calving rates. We have so far only considered temporal variability in ice-shelf mass and meltwater flux due to changes in ice-shelf basal melt rates relative to steady-state values. However, ice-shelf hydrofracture in the Antarctic Peninsula[85] and excess iceberg calving rates due to long-term dynamic thinning of Amundsen Sea[86] have also contributed to net ice-shelf mass loss and increases in meltwater export to the upper ocean in recent decades. We estimated net mass loss due to changes in ice-shelf extent from ice-shelf thickness estimates generated using elevations from the ERS-1 geodetic phase (1994–1995) for regions where ice-shelf areas decreased; these were excluded from previous thickness estimates[87]. We estimate a net mass loss of $1,650 \pm 200$ Gt from Antarctic Peninsula ice shelves during our record (Supplementary Fig. 7) due to the hydrofracture-induced collapse of Larsen A, Larsen B and sections of Wilkins ice shelves[88,89]. In addition, net retreat of Thwaites, Pine Island and Getz ice shelves in the Amundsen Sea contributed to a combined net mass loss of $1,230 \pm 70$ Gt. The combined mass loss from excess calving of Antarctic Peninsula and Amundsen Sea sector ice shelves was $2,880 \pm 210$ Gt, which is comparable to our circum-Antarctic mass loss estimate of $3,960 \pm 1,100$ Gt from thinning ice shelves (Fig. 3a).

Data availability
ERS-1, ERS-2, Envisat and CryoSat-2 radar altimetry data are available from the European Space Agency (ERS-1 and ERS-2 data from ftp://ra-ftp-ds.eo.esa.int/, Envisat data from ftp://ra2-ftp-ds.eo.esa.int/ and CryoSat-2 level-2 SARIn-mode data from ftp://science-pds.cryosat.esa.int/SIR_SIN_L2). We provide two datasets at https://doi.org/10.6075/J04Q7SHT: (1) basal melt rates at high spatial resolution, posted on a 500 m grid, for the period 2010–2018 and (2) changes in height from satellite altimetry, firn air content from GSFC-FDMv0 and precipitation minus evaporation from MERRA-2 at 10-km grid cells and three-month intervals for 1994–2018; (2) can be used to estimate time-varying basal melt rates using Equation (7).

Code availability
The Matlab, Python and shell scripts used for the analyses described in this study can be obtained from the corresponding author upon reasonable request. Code to read and visualize the derived data products described in this manuscript, and to reproduce the major elements of Figs. 1 to 4, is available at https://github.com/sioglaciology/ice_shelf_change.

References
51. Moholdt, G., Padman, L. & Fricker, H. A. Basal mass budget of Ross and Filchner-Ronne ice shelves, Antarctica, derived from Lagrangian analysis of ICESat altimetry. *J. Geophys. Res. Earth Surf.* **119**, 2361–2380 (2014).
52. Förste, C. et al. EIGEN-6C4 The latest combined global gravity field model including GOCE data up to degree and order 2190 of GFZ Potsdam and GRGS Toulouse (GFZ Data Services, 2014); http://doi.org/10.5880/icgem.2015.1
53. Andersen, O., Knudsen, P. & Stenseng, L. in *IGFS 2014* (eds Jin, S. & Barzaghi, R.) 111–121 (Springer, 2016).
54. Howard, S. L., Padman, L. & Erofeeva, S. Y. CATS2008: Circum-Antarctic Tidal Simulation version 2008 (USAP Data Center, 2019); https://doi.org/10.15784/601235
55. Padman, L., Fricker, H. A., Coleman, R., Howard, S. & Erofeeva, L. A new tide model for the Antarctic ice shelves and seas. *Ann. Glaciol.* **34**, 247–254 (2002).

56. Carrère, L. & Lyard, F. Modeling the barotropic response of the global ocean to atmospheric wind and pressure forcing—comparisons with observations. *Geophys. Res. Lett.* **30**, 1275 (2003).

57. Egbert, G. D. & Erofeeva, S. Y. Efficient inverse modeling of barotropic ocean tides. *J. Atmos. Ocean. Technol.* **19**, 183–204 (2002).

58. Rye, C. D. et al. Rapid sea-level rise along the Antarctic margins in response to increased glacial discharge. *Nat. Geosci.* **7**, 732–735 (2014).

59. Gardner, A. S. et al. Increased West Antarctic and unchanged East Antarctic ice discharge over the last 7 years. *Cryosphere* **12**, 521–547 (2018).

60. Rignot, E., Mouginot, J. & Scheuchl, B. *MEaSUREs InSAR-Based Antarctica Ice Velocity Map, Version 2* (NSIDC, 2017); https://nsidc.org/data/NSIDC-0484/versions/2

61. Adusumilli, S. et al. Variable basal melt rates of Antarctic Peninsula ice shelves, 1994–2016. *Geophys. Res. Lett.* **45**, 4086–4095 (2018).

62. Alley, K. E. et al. Continent-wide estimates of Antarctic strain rates from Landsat 8-derived velocity grids. *J. Glaciol.* **64**, 321–332 (2018).

63. Gelaro, R. et al. The modern-era retrospective analysis for research and applications, version 2 (MERRA-2). *J. Clim.* **30**, 5419–5454 (2017).

64. Arthern, R. J., Vaughan, D. G., Rankin, A. M., Mulvaney, R. & Thomas, E. R. In situ measurements of Antarctic snow compaction compared with predictions of models. *J. Geophys. Res. Earth Surf.* **115**, F03011 (2010).

65. Stevens, C. M. et al. The Community Firn Model (CFM) v1.0. Preprint at https://doi.org/10.5194/gmd-2019-361 (2020).

66. Morlighem, M. et al. Deep glacial troughs and stabilizing ridges unveiled beneath the margins of the Antarctic ice sheet. *Nat. Geosci.* **13**, 132–137 (2020).

67. Boyer, T. P. et al. *World Ocean Database (WOD) 2018* (NCEI, 2018); https://www.nodc.noaa.gov/OC5/WOD/pr_wod.html

68. McDougall, T. J., Barker, P. M., Feistel, R. & Galton-Fenzi, B. K. Melting of ice and sea ice into seawater and frazil ice formation. *J. Phys. Oceanogr.* **44**, 1751–1775 (2014).

69. McDougall, T. J. & Barker, P. M. *Getting Started with TEOS-10 and the Gibbs Seawater (GSW) Oceanographic Toolbox* (SCOR/IAPSO, 2011).

70. Schaffer, J. et al. A global, high-resolution data set of ice sheet topography, cavity geometry, and ocean bathymetry. *Earth Syst. Sci. Data.* **8**, 543–557 (2016).

71. Dunn, J. R. & Ridgway, K. R. Mapping ocean properties in regions of complex topography. *Deep Sea Res. Part I* **49**, 591–604 (2002).

72. Dinniman, M. S., Klinck, J. M. & Smith, W. O. A model study of circumpolar deep water on the West Antarctic Peninsula and Ross Sea continental shelves. *Deep Sea Res. Part II* **58**, 1508–1523 (2011).

73. Brockley, D. J. et al. REAPER: reprocessing 12 years of ERS-1 and ERS-2 altimeters and microwave radiometer data. *IEEE Trans. Geosci. Remote Sens.* **55**, 5506–5514 (2017).

74. Soussi, B. et al. *ENVISAT Altimetry Level 2 Product Handbook* (ESA, 2018).

75. Paolo, F. S., Fricker, H. A. & Padman, L. Constructing improved decadal records of Antarctic ice shelf height change from multiple satellite radar altimeters. *Remote Sens. Environ.* **177**, 192–205 (2016).

76. Wessem, J. M. et al. Modelling the climate and surface mass balance of polar ice sheets using RACMO2—Part 2: Antarctica (1979–2016). *Cryosphere* **12**, 1479–1498 (2018).

77. Nicolas, J. P. et al. January 2016 extensive summer melt in West Antarctica favoured by strong El Niño. *Nat. Commun.* **8**, 15799 (2017).

78. McMillan, M. et al. Increased ice losses from Antarctica detected by CryoSat-2. *Geophys. Res. Lett.* **41**, 3899–3905 (2014).

79. Mouginot, J., Rignot, E. & Scheuchl, B. Sustained increase in ice discharge from the Amundsen Sea Embayment, West Antarctica, from 1973 to 2013. *Geophys. Res. Lett.* **41**, 1576–1584 (2014).

80. Mouginot, J., Rignot, E., Scheuchl, B. & Millan, R. Comprehensive annual ice sheet velocity mapping using Landsat-8, Sentinel-1, and RADARSAT-2 data. *Remote Sens.* **9**, 364 (2017).

81. Ligtenberg, S. R. M., Helsen, M. M. & Broeke, M. Rvanden An improved semi-empirical model for the densification of Antarctic firn. *Cryosphere* **5**, 809–819 (2011).

82. Joughin, I. & Vaughan, D. G. Marine ice beneath the Filchner–Ronne Ice Shelf, Antarctica: a comparison of estimated thickness distributions. *Ann. Glaciol.* **39**, 511–517 (2004).

83. Fricker, H. A., Popov, S., Allison, I. & Young, N. Distribution of marine ice beneath the Amery Ice Shelf. *Geophys. Res. Lett.* **28**, 2241–2244 (2001).

84. Lambrecht, A., Sandhäger, H., Vaughan, D. G. & Mayer, C. New ice thickness maps of Filchner–Ronne Ice Shelf, Antarctica, with specific focus on grounding lines and marine ice. *Antarct. Sci.* **19**, 521–532 (2007).

85. Cook, A. J. & Vaughan, D. G. Overview of areal changes of the ice shelves on the Antarctic Peninsula over the past 50 years. *Cryosphere* **22** (2010).

86. MacGregor, J. A., Catania, G. A., Markowski, M. S. & Andrews, A. G. Widespread rifting and retreat of ice-shelf margins in the eastern Amundsen Sea Embayment between 1972 and 2011. *J. Glaciol.* **58**, 458–466 (2012).

87. Griggs, J. A. & Bamber, J. L. Antarctic ice-shelf thickness from satellite radar altimetry. *J. Glaciol.* **57**, 485–498 (2011).

88. Scambos, T. A., Bohlander, J. A., Shuman, C. A. & Skvarca, P. Glacier acceleration and thinning after ice shelf collapse in the Larsen B embayment, Antarctica. *Geophys. Res. Lett.* **31**, L18402 (2004).

89. Scambos, T. et al. Ice shelf disintegration by plate bending and hydro-fracture: satellite observations and model results of the 2008 Wilkins ice shelf break-ups. *Earth Planet. Sci. Lett.* **280**, 51–60 (2009).

Author contributions
S.A., H.A.F., L.P. and M.R.S. conceptualized the study. S.A. and M.R.S. performed altimetry data processing. B.M. conducted climate and firn modelling. All authors contributed to the writing and editing of the manuscript. H.A.F., B.M., L.P. and M.R.S. contributed equally to this work.

Competing interests
The authors declare no competing interests.

Additional information
Supplementary information is available for this paper at https://doi.org/10.1038/s41561-020-0616-z.

Correspondence and requests for materials should be addressed to S.A.
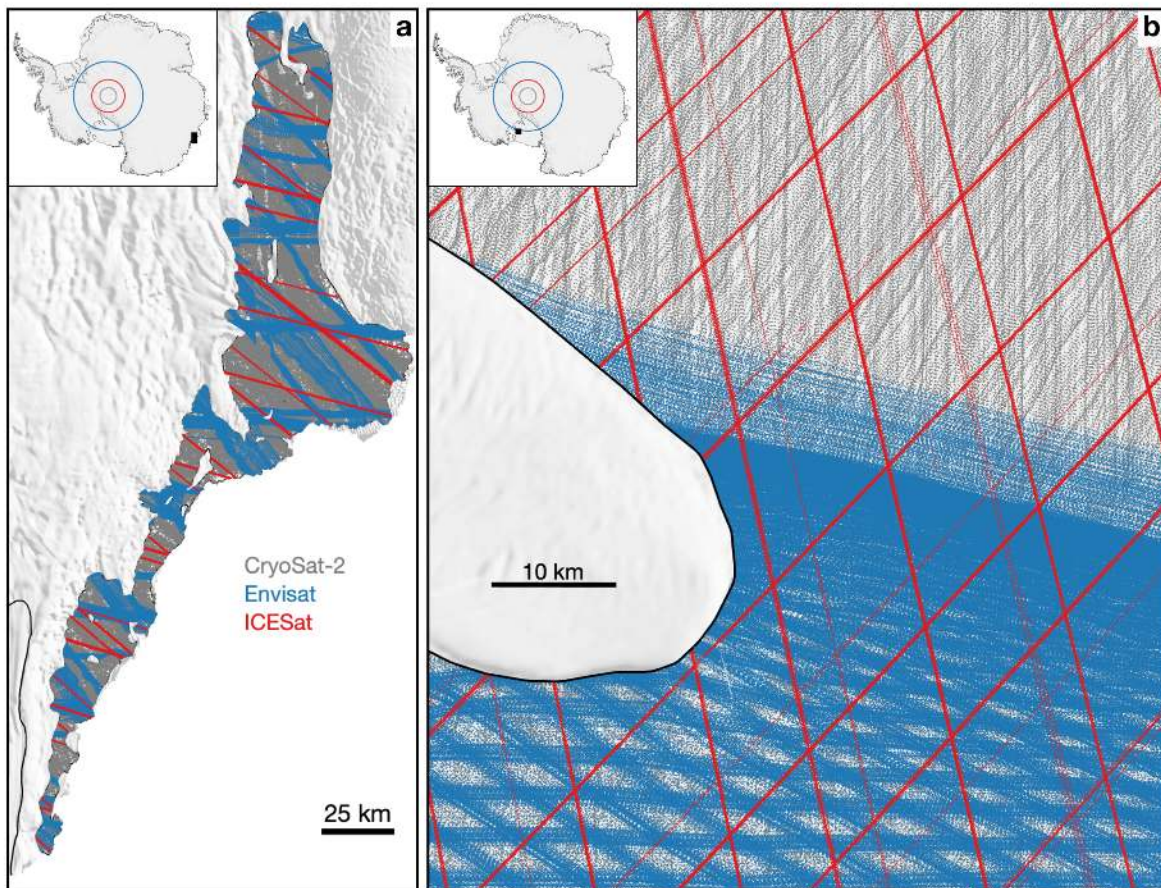
Peer review information Primary Handling Editors: James Super; Heike Langenberg.

**Reprints and permissions information** is available at www.nature.com/reprints.

In the format provided by the authors and unedited.

Interannual variations in meltwater input to the Southern Ocean from Antarctic ice shelves

In the format provided by the authors and unedited

Supplementary Figure 1: Spatial sampling of satellite laser and radar altimeters. Spatial sampling of heights measured using CryoSat-2 (2010–present), Envisat (2002–2012), and ICESat (2003–2009) altimetry over (a) Totten Ice Shelf, East Antarctica, and (b) Ross Ice Shelf. The southern orbit limit of Envisat is visible in (b), and the orbit limits for the three altimeters are shown in the inset figures, with locations of each site shown by the black box. Some Envisat tracks sampled areas slightly south of its nominal orbit limit (81.5°S) during Phase 3 from 2010 until the end of its mission in 2012.
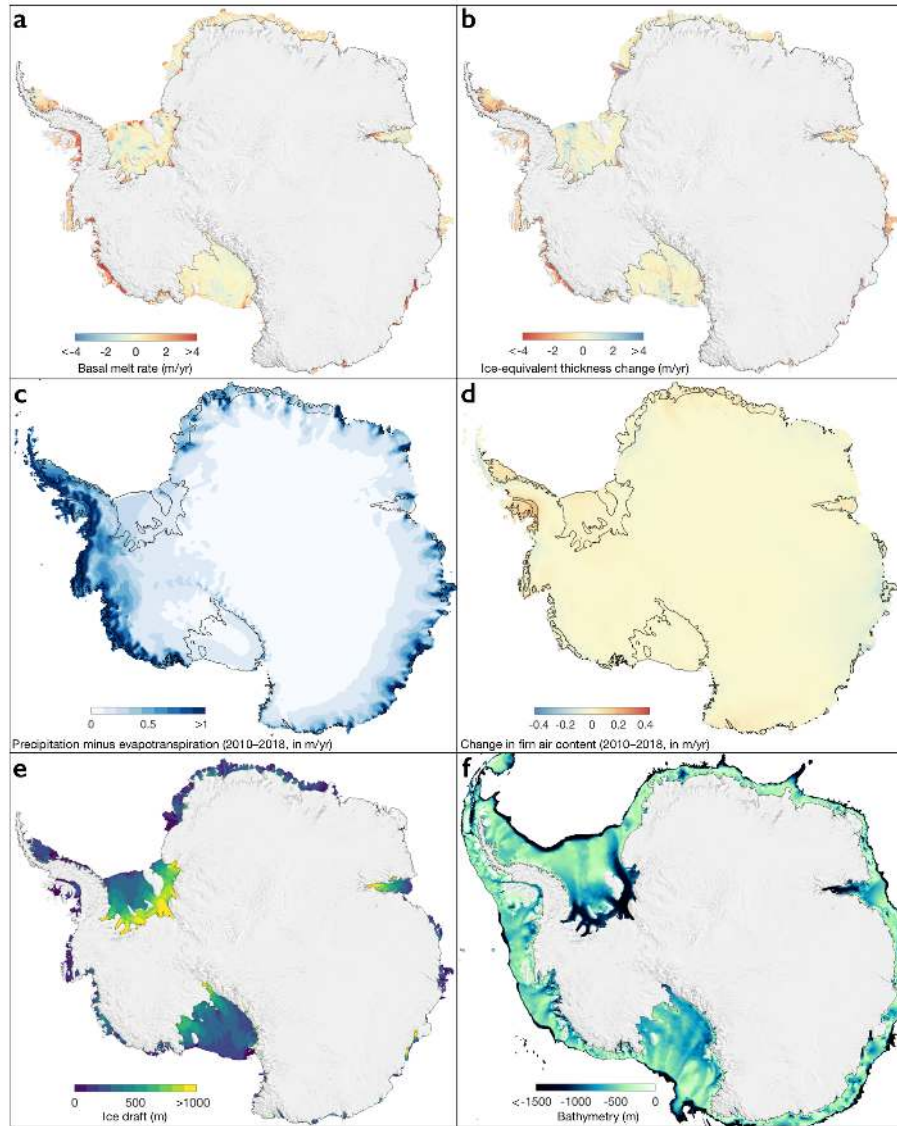
Supplementary Figure 2: Key ice observations across Antarctic ice shelves. Panels (a–e) are for the CryoSat-2 (2010–2018) period. (a) High resolution ice shelf basal melt rates in m of ice equivalent per year (same values as Figure 1, with a different color scale); (b) ice-equivalent thickness change in m of ice equivalent per year; (c) precipitation minus evapotranspiration in m of ice equivalent per year; (d) change in firn air content in m of air per year; (e) ice draft from CryoSat-2 with data gaps filled in using BedMachine[67]; and (f) bathymetry around Antarctica from BedMachine. Color range for (d) is scaled to be consistent with the scale for (a,b) after hydrostatic adjustment (red values indicate a positive change in firn air content).
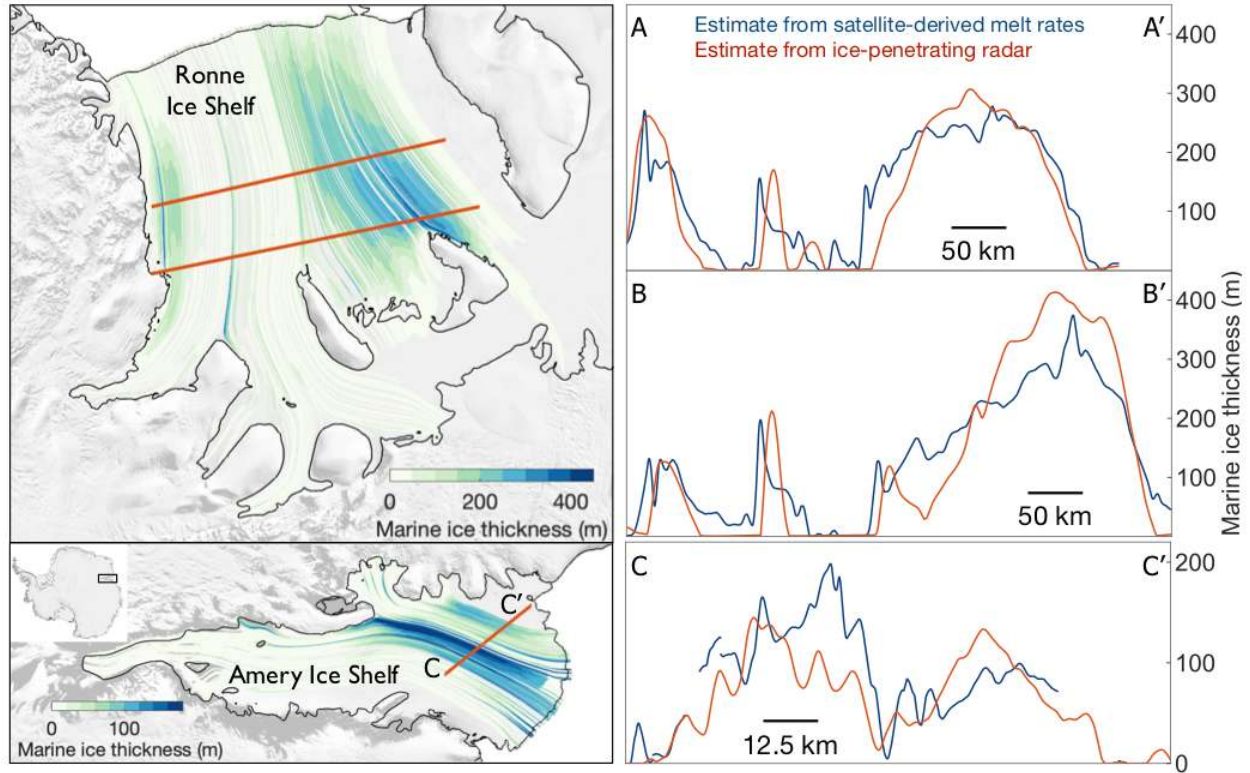
Supplementary Figure 3: Estimates of marine-ice thickness. Marine-ice thickness under Ronne and Amery ice shelves estimated using satellite-derived steady-state basal melt rates (left) using the methodology of ref. [83] described in Section S7. We used bicubic interpolation to extract values along three profiles (A-A', B-B', C-C') to compare them against independent estimates from airborne radar sounding from refs. [84,85].
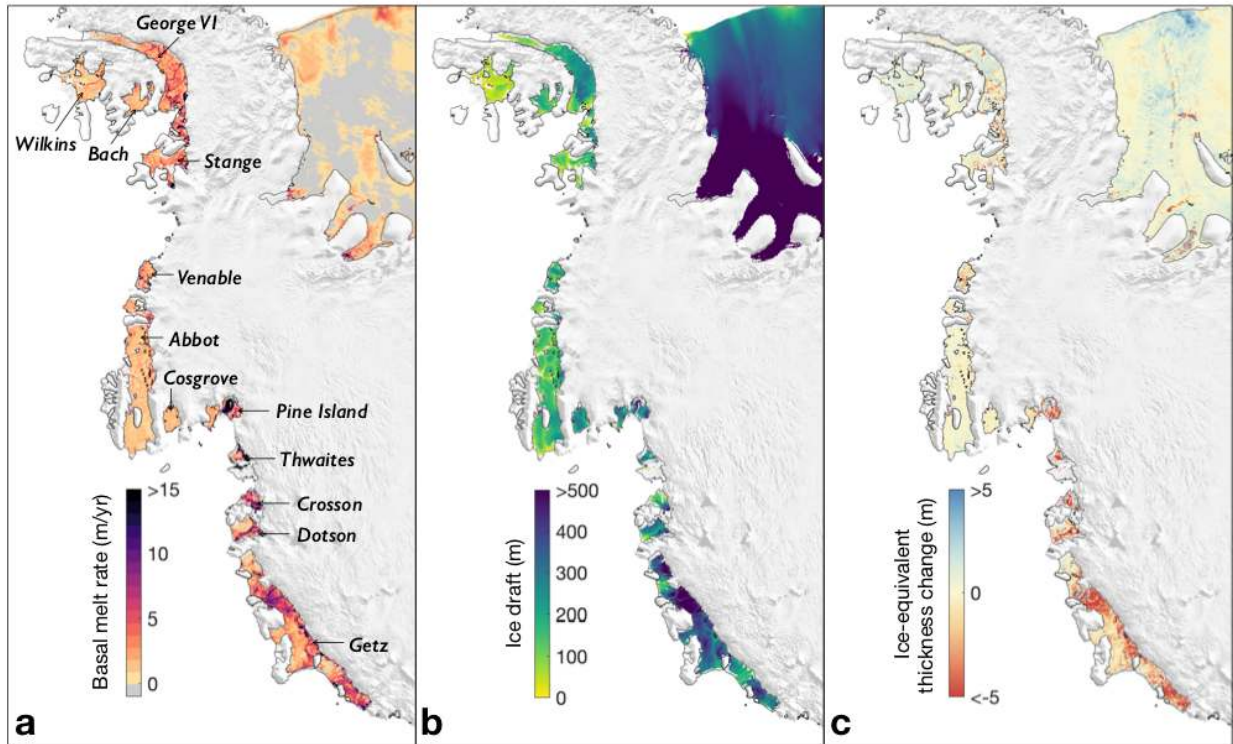
Supplementary Figure 4: Key ice observations of Amundsen and Bellingshausen Sea ice shelves. Amundsen Sea and Bellingshausen Sea ice shelf (a) basal melt rates in m of ice equivalent per year, (b) ice draft, and (c) thickness change in m of ice equivalent per year for the CryoSat-2 period (2010–2018). Individual ice shelves are identified on panel (a).
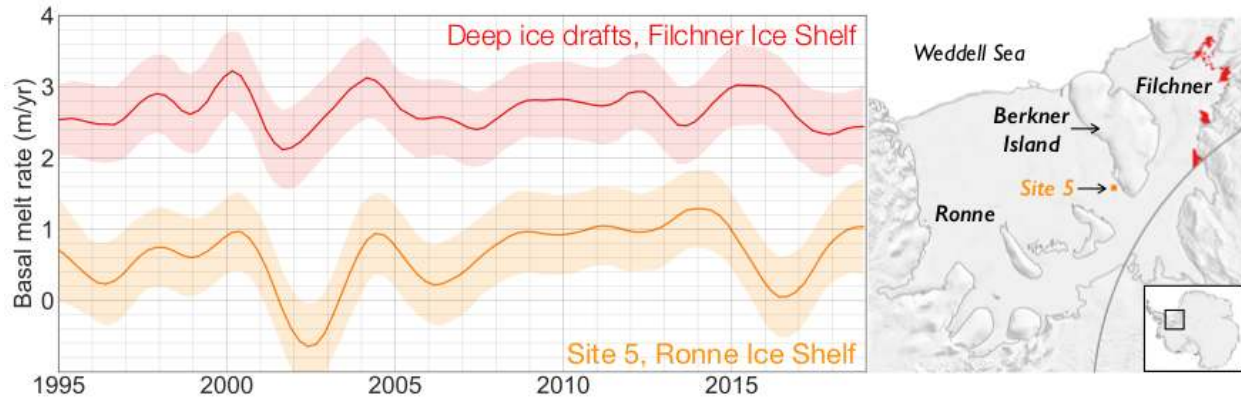
Supplementary Figure 5: Basal melt rates at Site 5. Basal melt rates at deep ice drafts for Filchner Ice Shelf and at observation Site 5 near the southwestern Berkner Island coast of Ronne Ice Shelf. Temporal variations of basal melting in both regions are influenced by processes in the Weddell Sea north of the ice shelves, but are not directly linked[40]. Time series are smoothed with a low-pass filter with a three-year cutoff.
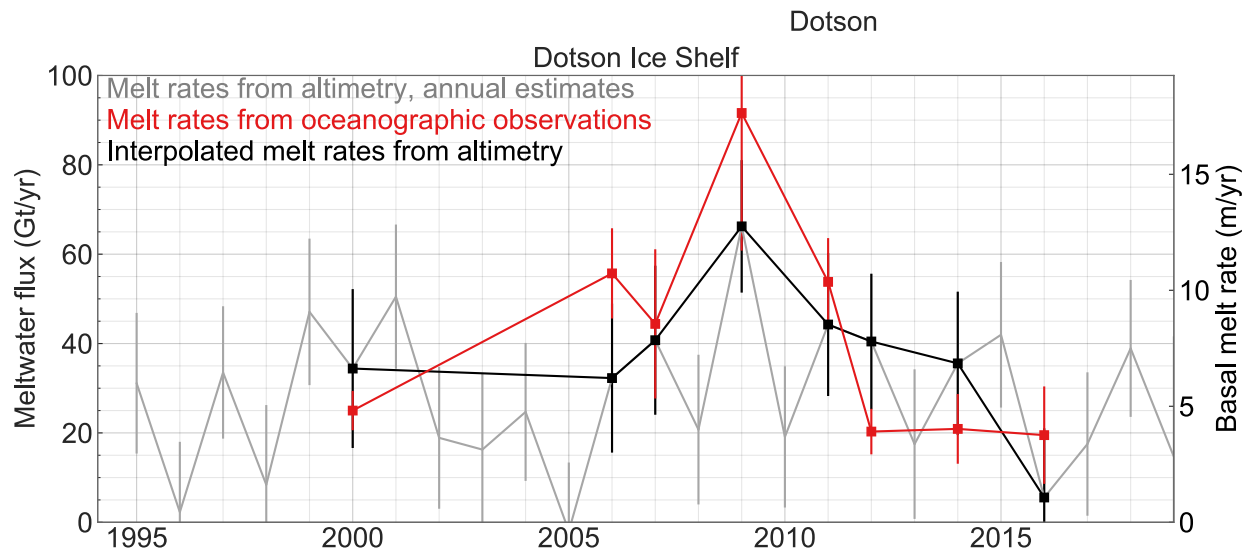
Supplementary Figure 6: Basal melt rates for Dotson Ice Shelf. Satellite-derived annual basal melt rates (in gray) for Dotson Ice Shelf (see Figure S4a for location) from this study compared to estimates from eight oceanographic sections near the ice front (in red)[4]. To aid visual comparison, we interpolated (in black) the raw time series to the timestamps of the oceanographic measurements.
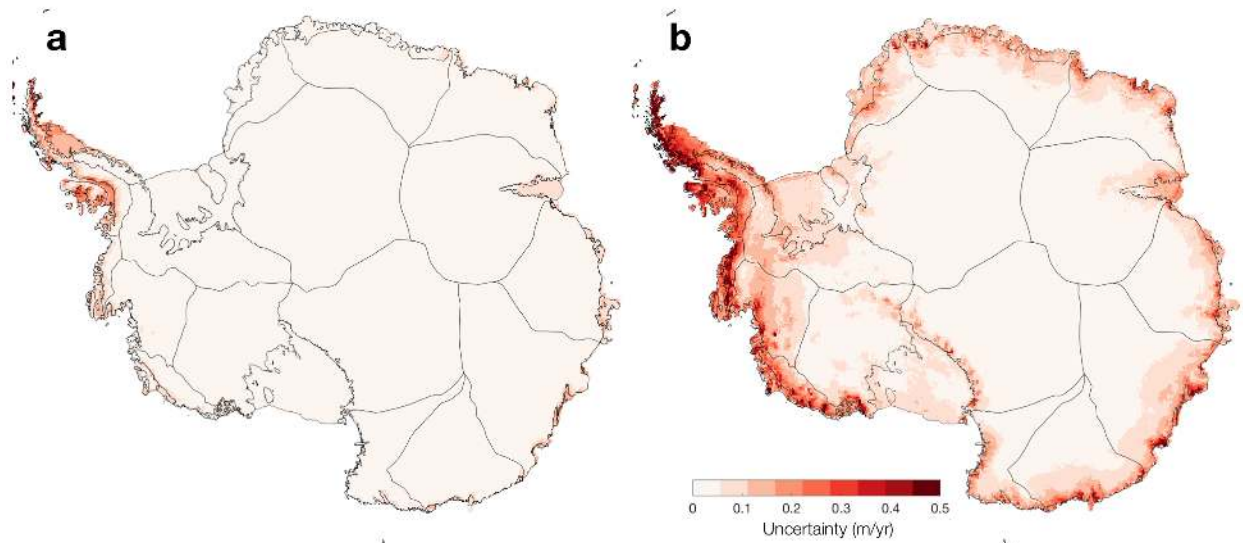
Supplementary Figure 7: Uncertainties in changes in firn air content. Uncertainties in changes in firn air content in m of firn air per year at annual time scales. (a) Uncertainty from steady-state assumption in climate for firn model spin-up[1]. (b) Uncertainty arising from resolution and errors in model physics, estimated as the differences between the outputs from the GSFC-FDMv0 (forced by the MERRA-2 atmospheric model with mean climate from the M2R12K replay) and the IMAU firn densification model forced by the RACMO2.3p2 regional atmospheric model[82]. Grounded-ice basins are from ref. [91]. These uncertainties represent an upper bound and are lower at the longer time scales typically considered in this study.
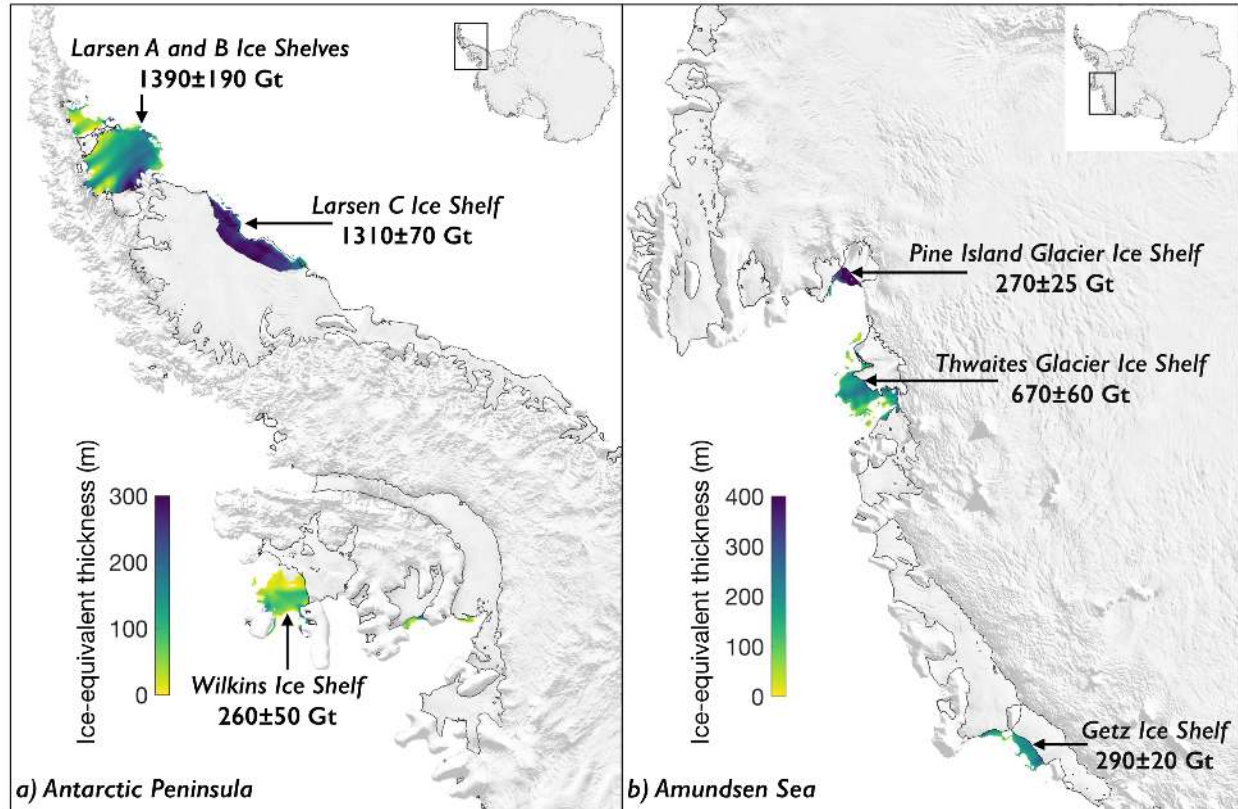
Supplementary Figure 8: Changes in extent of Antarctic Peninsula and Amundsen Sea sector ice shelves. 1994–2018. Ice-equivalent thickness data from the ERS-1 geodetic phase (1994/1995) are shown for regions that were covered by open ocean or sea ice at any time during the CryoSat-2 period. We only show regions with heights above mean sea level greater than 10 m (Figure 1).

Ice Shelf	Area (km²)	Latitude	Longitude	Basal melt rate, 1994–2018 (m/yr)	Meltwater flux, 1994–2018 (Gt/yr)	Excess meltwater flux, 1994–2018 (Gt/yr)	Meltwater flux, 2010–2018 (Gt/yr)
George VI	22755	-72.39	-70.24	4.3 ± 2.2	88.8 ± 45.7	16.4 ± 45.7	82.4 ± 45.7
Bach	4444	-72.05	-71.82	3.2 ± 2.1	13.1 ± 8.5	3.2 ± 8.5	11.8 ± 8.5
Wilkins	10390	-70.40	-71.73	2.7 ± 3.4	26.1 ± 32.0	2.5 ± 32.0	23.2 ± 32.0
Stange	7397	-73.29	-76.64	3.7 ± 2.1	25.4 ± 14.2	7.2 ± 14.2	25.9 ± 14.2
Venable	3037	-73.11	-87.33	5.1 ± 2.0	14.3 ± 5.5	7.6 ± 5.6	10.3 ± 5.5
Abbot	27461	-72.94	-94.78	1.5 ± 1.5	37.1 ± 38.1	8.5 ± 38.1	37.9 ± 38.2
Bellingshausen	**75484**	**–**	**–**	**3.0 ± 1.0**	**204.8 ± 69.7**	**45.3 ± 69.7**	**191.4 ± 69.7**
Cosgrove	2964	-73.56	-100.33	1.0 ± 1.5	2.7 ± 4.1	0.0 ± 4.1	4.2 ± 4.1
Pine Island	5950	-74.83	-100.79	14.0 ± 1.6	76.6 ± 8.6	15.8 ± 8.6	76.0 ± 8.7
Thwaites	3352	-75.08	-106.16	26.7 ± 2.4	81.9 ± 7.4	11.6 ± 7.4	81.1 ± 7.4
Crosson	2932	-75.03	-110.51	7.8 ± 1.8	20.9 ± 4.9	10.8 ± 4.9	17.9 ± 4.9
Dotson	5657	-74.70	-112.92	5.4 ± 1.6	28.2 ± 8.5	13.6 ± 8.5	26.1 ± 8.5
Getz	32114	-74.46	-124.49	4.2 ± 1.4	124.1 ± 40.9	61.4 ± 40.9	122.6 ± 40.9
Amundsen	**52969**	**–**	**–**	**6.9 ± 0.9**	**334.5 ± 43.7**	**113.2 ± 43.7**	**327.9 ± 43.8**
Land	587	-75.58	-141.43	20.4 ± 2.7	11.0 ± 1.5	2.3 ± 1.5	10.9 ± 1.5
Nickerson	6001	-75.81	-145.84	1.2 ± 1.4	6.5 ± 7.9	-0.1 ± 7.9	8.0 ± 7.9
Sulzberger	11229	-77.08	-148.58	1.5 ± 1.3	15.7 ± 13.3	1.6 ± 13.3	18.5 ± 13.3
Withrow	341	-77.15	-157.17	3.3 ± 1.8	1.0 ± 0.6	0.0 ± 0.6	0.9 ± 0.6
Ross West	198293	-80.37	-160.13	0.3 ± 0.4	45.8 ± 68.3	-32.4 ± 68.3	26.6 ± 69.2
Ross East	135261	-80.70	168.59	0.3 ± 0.4	34.3 ± 45.2	-40.2 ± 45.2	31.0 ± 45.3
Drygalski	2168	-75.38	163.16	1.9 ± 0.9	3.8 ± 1.7	0.5 ± 1.7	3.8 ± 1.7
Nansen	1835	-74.86	163.15	1.6 ± 1.1	2.8 ± 1.8	-0.3 ± 1.8	2.2 ± 1.8
Mariner	2354	-73.32	168.09	1.1 ± 1.7	2.3 ± 3.6	-0.3 ± 3.6	2.4 ± 3.6
Ross	**358068**	**–**	**–**	**0.4 ± 0.3**	**123.3 ± 83.5**	**-68.7 ± 83.5**	**104.3 ± 84.2**
Moscow University	4145	-66.88	121.07	7.4 ± 2.1	28.3 ± 8.0	3.8 ± 8.0	25.8 ± 8.0
Rennick	3123	-70.61	161.69	1.9 ± 1.4	5.5 ± 3.9	1.3 ± 3.9	5.7 ± 3.9
Cook	3408	-68.54	152.78	1.3 ± 1.6	3.9 ± 5.1	-1.0 ± 5.1	4.6 ± 5.1
Mertz	3243	-67.30	145.19	5.0 ± 2.4	14.8 ± 7.1	1.2 ± 7.1	13.8 ± 7.1
Holmes	1717	-66.76	127.26	13.3 ± 2.9	20.9 ± 4.5	0.6 ± 4.5	17.7 ± 4.5
Totten	6078	-67.05	116.12	11.5 ± 2.0	64.0 ± 11.0	8.4 ± 11.0	59.4 ± 11.0
Shackleton	26182	-66.06	97.90	1.8 ± 1.9	44.0 ± 44.8	12.8 ± 44.8	40.7 ± 44.8
West	15306	-66.96	85.00	1.4 ± 1.8	20.1 ± 25.1	2.9 ± 25.1	15.7 ± 25.1
Wilkes	**63202**	**–**	**–**	**3.5 ± 0.9**	**201.4 ± 54.1**	**30.0 ± 54.1**	**183.5 ± 54.1**
Amery	**60228**	**–**	**–**	**0.8 ± 0.7**	**45.6 ± 40.0**	**-2.5 ± 40.0**	**48.9 ± 39.9**
Prince Harald	4067	-69.24	35.25	2.3 ± 1.9	8.6 ± 7.2	0.1 ± 7.2	7.4 ± 7.1
Brunt_Stancomb	34573	-75.10	-22.51	0.6 ± 0.8	18.0 ± 24.6	0.2 ± 24.6	17.3 ± 24.7
Riiser-Larsen	42644	-72.91	-15.31	0.5 ± 0.8	19.4 ± 30.0	3.2 ± 30.0	16.2 ± 30.0
Quar	2076	-71.20	-10.86	0.4 ± 0.8	0.7 ± 1.6	0.2 ± 1.6	0.9 ± 1.6
Ekstrom	6754	-71.05	-8.55	1.0 ± 1.2	6.4 ± 7.2	1.0 ± 7.2	6.4 ± 7.2
Baudouin	32789	-69.96	28.47	1.0 ± 1.0	28.8 ± 29.1	0.8 ± 29.1	34.5 ± 29.1
Borchgrevink	21368	-70.32	20.38	0.8 ± 1.0	15.5 ± 20.3	3.0 ± 20.3	14.4 ± 20.3
Lazarev	8456	-69.92	14.45	0.8 ± 0.8	6.3 ± 6.2	1.9 ± 6.2	7.4 ± 6.3
Fimbul	40600	-70.57	1.55	1.0 ± 0.8	36.2 ± 29.0	-0.5 ± 29.0	32.7 ± 29.1
Nivl	7275	-70.25	11.29	1.1 ± 1.1	7.0 ± 7.2	0.6 ± 7.2	7.4 ± 7.2
Vigrid	2071	-70.23	8.33	1.2 ± 1.0	2.3 ± 1.8	0.2 ± 1.8	2.3 ± 1.9
Atka	1780	-70.61	-6.84	1.0 ± 1.2	1.6 ± 1.9	0.3 ± 1.9	1.5 ± 1.9
Jelbart	10756	-70.97	-4.33	1.0 ± 1.1	9.9 ± 11.3	1.6 ± 11.3	9.9 ± 11.3
Queen Maud	**215208**	**–**	**–**	**0.8 ± 0.3**	**160.7 ± 62.8**	**12.6 ± 62.8**	**158.4 ± 62.8**
Ronne	311968	-78.96	-65.57	0.2 ± 0.4	47.2 ± 119.3	10.5 ± 119.3	21.2 ± 119.9
Filchner	83304	-80.56	-41.02	0.4 ± 0.4	34.2 ± 29.6	-1.3 ± 29.6	33.5 ± 29.6
Filchner-Ronne	**395271**	**–**	**–**	**0.2 ± 0.3**	**81.4 ± 122.9**	**9.2 ± 122.9**	**54.8 ± 123.5**
Larsen D	18282	-70.72	-61.64	1.8 ± 1.9	30.8 ± 31.3	3.9 ± 31.3	35.3 ± 31.8
Larsen C	42384	-67.33	-63.44	2.0 ± 2.5	77.9 ± 98.7	15.9 ± 98.7	64.6 ± 98.8
Larsen B	1985	-65.87	-61.82	2.2 ± 2.3	3.9 ± 4.2	1.6 ± 4.2	3.9 ± 4.2
Larsen	**75800**	**–**	**–**	**1.6 ± 1.5**	**112.7 ± 103.6**	**21.4 ± 103.6**	**103.8 ± 103.8**
All ice shelves	**1296230**	**–**	**–**	**1.1 ± 0.1**	**1264.3 ± 147.4**	**160.5 ± 147.4**	**1173.1 ± 148.5**

Supplementary Table 1: Basal melt rates (in m/yr) and meltwater fluxes (in Gt/yr) of ice shelves surveyed in this study. Steady-state mass fluxes can be estimated as the difference between the mean mass flux between 1994 and 2018 and the excess mass flux during the same period. Uncertainties are 95% confidence intervals.